UrineSpec: A Lightweight Near-Infrared Spectroscopy System for Metabolite Detection in Urine

Mengyao Chen
Northwest University, IoT Research Center-Northwest University
China
chenmy@stumail.nwu.edu.cn

Hao Chen
Northwest University, IoT Research Center-Northwest University
China
chh@stumail.nwu.edu.cn

Siying Niu*
Northwest University, Shaanxi International Joint Research Centre for the Battery-Free IoT
China
niusy@nwu.edu.cn

ABSTRACT

Urine concentration levels of important biomarkers offer valuable insights for the detection of chronic diseases. However, existing detection methods are hindered by high costs or limited performance, preventing long-term monitoring of urine components in domestic settings. This paper introduces UrineSpec, a low-cost, lightweight system using near-infrared (NIR) light for precise detection of trace macromolecules in urine. It proposes a novel method that recovers accurate multi-absorption features from coarse optical responses to obtain fine-grained spectra. Based on this, we manage to extract the absorption spectrum of the substance from the complex mixed spectra and achieve accurate concentration identification. Extensive experimental results indicate that UrineSpec can monitor five concentration levels of three important biomarkers with an accuracy of uric acid, albumin and glucose over 98.4%, 98.8% and 98.6% respectively. This high level of precision underscores the potential of UrineSpec as an effective tool for non-invasive chronic disease monitoring and early intervention.

CCS CONCEPTS

• **Applied computing** → **Consumer health**; • **Human-centered computing** → *Ubiquitous and mobile computing systems and tools.*

KEYWORDS

Urine sensing, Near-Infrared spectrometer, Spectral recovery, Lightweight system, Internet of Things(IoT)

ACM Reference Format:
Mengyao Chen, Hao Chen, and Siying Niu. 2024. UrineSpec: A Lightweight Near-Infrared Spectroscopy System for Metabolite Detection in Urine. In *The 22nd ACM Conference on Embedded Networked Sensor Systems (SENSYS '24), November 4–7, 2024, Hangzhou, China.* ACM, New York, NY, USA, 12 pages. https://doi.org/10.1145/3666025.3699375

*Corresponding author.

SenSys'24, November 4-7, 2024, Hangzhou, China

ACM ISBN 979-8-4007-0697-4/24/11
https://doi.org/10.1145/3666025.3699375

1 INTRODUCTION

Urine is a vital metabolic indicator that reflects the body's health status, playing a crucial role in early screening, diagnosis, and prevention of chronic diseases[1–4]. For instance, uric acid (UA) levels in urine are significant predictors[5]; research shows that every 60 μmol increase in UA raises the risk of diabetes by 17% and hypertension by 15% to 23%[6]. Similarly, elevated protein levels can indicate chronic kidney disease, which has a high prevalence of 10.8% but a low awareness rate of only 12.5%[7]. Additionally, the presence of glucose (GLU) in urine directly signifies diabetes, a major health concern affecting approximately 537 million adults globally as of 2021[8]. Therefore, continuous and long-term monitoring of urine allows for the timely detection of chronic diseases, significantly reducing their prevalence and improving the quality of human life.

Traditional urine testing requires a hospital visit and specialized equipment, resulting in high time and test costs and inability to continuously monitor chronic diseases. Other methods, such as urine analysis test strips[9, 10] and home urinalysis devices[11], use dry chemical methods but suffer from lower stability, accuracy, and high consumable costs. Modern methods using advanced technology improve efficiency and convenience. For example, electrochemical and biosensors[12–14] with near-field communication technology offer new potential for sustainable monitoring but are sensitive to environmental factors which give rise to false positive results. Therefore, there is a pressing need for a highly accurate and easy-to-use urine testing method that can be applied for long-term testing regardless of testing scenarios and environmental constraints.

Inspired by recent progress on wireless sensing, utilizing wireless signals for urine detection makes testing more convenient, and suitable for long-term monitoring[15–17]. However, measurement of liquids based on wireless signals is mainly divided into two principles[18]: one is the transmission method, which requires vessel size to be large enough to wireless signal transmit through otherwise the signal will diffract and cause errors; the other is the reflection method, which can only qualitatively analyse the liquid but not quantitatively analyse the composition of the liquid. In view of this, wireless signals have limitations in measuring urine metabolism. Hence, we have discovered that light, as an electromagnetic wave with ultra-high frequency, can easily penetrate small urine samples, offering advantages such as selective absorption and fine-grained sensing. However, conventional spectrometers are costly and bulky, while simpler, low-cost optical sensing methods provide only qualitative analysis and limited performance. Consequently, despite optical signals being ideal for molecular-level substance

Figure 1: Schematic application of UrineSpec in a home scenario.

detection, achieving affordable, high-precision multi-component urine analysis remains challenging.

In this paper, we introduce UrineSpec, a low-cost spectral system designed to detect changes in light transmission caused by vibrations in molecular structures under near-infrared (NIR) radiation. By analyzing these changes, UrineSpec can estimate the composition and concentration of various urine components. The core concept of UrineSpec is to enhance the performance limitations of data caused by low-cost devices without increasing hardware costs, and to overcome interferences to accurately identify multiple components in urine. As shown in Fig. 1, UrineSpec is easily applicable for urine monitoring in daily life. However, developing this system presents the following challenges.

- Extracting features from weak signals is challenging. The emission light source for this system is a cheap LED, whose power is three orders of magnitude lower compared to the laser of a professional spectrometer, resulting in weak signals and coarse data. Moreover, urine is mixed solution 95% composed of water the rest being various metabolites, where the background peaks due to water absorption need to be distinguished from the characteristic peaks to ensure spectral accuracy.
- Obtaining detailed spectra is challenging. The system uses a photo-detector at the receiving end, and it is very difficult to recover the single data we received from it into a continuous spectrum. Additionally, the NIR absorption of components in urine is characterized by broad absorption peaks and overlapping spectral bands. Scattering effects from non-uniform particles in the urine can lead to shifts in absorption values, which are far from the ideal spectrum.

To overcome these challenges, we first analyzed the principles of NIR absorption and modeled the components to be measured with NIR light, then designed a light sensing system and optimized it to improve its ability to sense weak signals. Secondly, utilizing the response properties of photodiodes and combine them with a multidimensional data spectral matrix approach to obtain multidimensional spectral values from a single received data, which method allows us to obtain a spectrum closer to the ideal and more accurate data. After that, we obtained high-quality spectral data to accurately estimate the concentrations of multiple constituents.

We designed and built the UrineSpec prototype for our experiments, costing less than $100. We evaluated UrineSpec on its ability to detect three important substances in urine: uric acid (UA), albumin (ALB), and glucose (GLU). Extensive results show that UrineSpec achieves more than 96% accuracy in detecting five concentration levels of UA or ALB or GLU, and achieves sensing resolutions of 0.5 $mmol/L$, 0.1 $\mu mol/L$, 0.5 $mmol/L$ for UA, ALB, and GLU, respectively. Its sensing resolution meets medical requirements for health level prediction.

To summarize, we make the following contributions:

- We propose a new light absorption sensing method based on a NIR molecular vibration mechanism. We design and implement a compact and low-cost prototype to simultaneously estimate UA, GLU, and ALB content in urine using off-the-shelf hardware components.
- We present a method to recover multidimensional spectral information from coarse photodiode response values. Without adding or changing any hardware components, achieving low-cost acquisition of fine-grained spectra.
- We conducted experiments with a large number of samples and tested real urine samples from actual users, proving its accuracy and robustness in measuring concentration levels in real-world scenarios.

2 BACKGROUND AND MOTIVATION

Background of the NIR spectra. Near-infrared (NIR) spectroscopy[19, 20], utilizing wavelengths from 780 to 2500 nm, effectively analyzes chemical substances by leveraging the interaction of NIR light with molecular vibrations, particularly those involving hydrogen-containing groups. This interaction produces distinctive absorption bands that closely reflect the molecular structure, facilitating both qualitative and quantitative analyses[21–23]. Furthermore, the quantification process in NIR spectroscopy follows Lambert-Beer's Law[24, 25], which states that the absorbance of light is directly proportional to the concentration of absorbing molecules in the sample. This principle allows for the precise determination of various components in biological samples, such as uric acid, urine protein, and glucose. As is well know, traditional spectroscopy methods[26, 27] are often expensive and complex to operate. They require specialized, high-cost equipment confined to laboratory settings and trained personnel to operate them, making them impractical for routine or everyday use.

Motivation. Our goal is to develop an affordable and intuitive optical system using readily available components, capable of acquiring spectral data for the analysis of urine composition levels. In the forthcoming sections, we will clarify the design and underlying concepts of the system, provide details on its implementation, and present evaluation results derived from comprehensive experiments.

3 SYSTEM DESIGN

In this section, we first establish a perception system based on the principle of NIR light absorption and discuss methods to eliminate water interference. Next, we detail how to recover fine-grained spectra from rough response data. Finally, we introduce methods

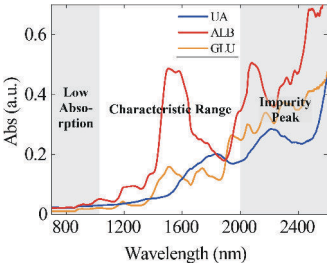

Figure 2: Absorption characteristics of UA, ALB, and GLU in the NIR light region.

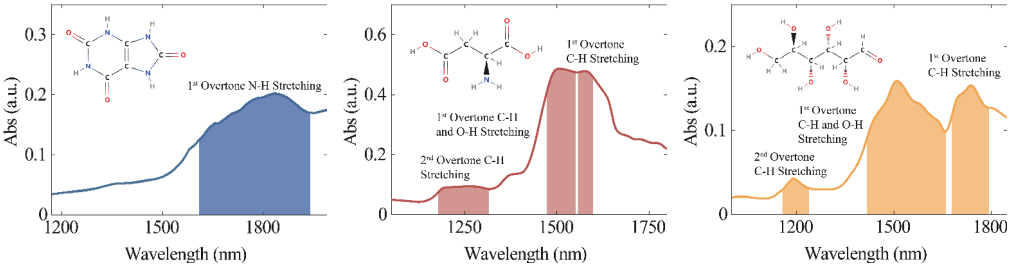

(a) UA (b) ALB (c) GLU

Figure 3: Molecular structure and absorption peaks of three substances.

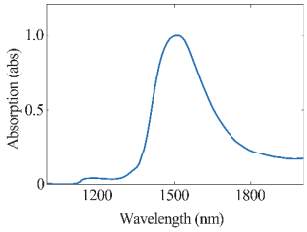

Figure 4: Absorption characteristics of water.

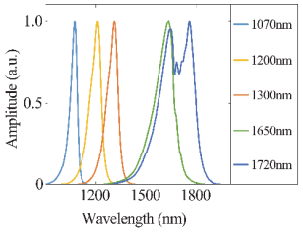

Figure 5: The spectral distribution of UrineSpec.

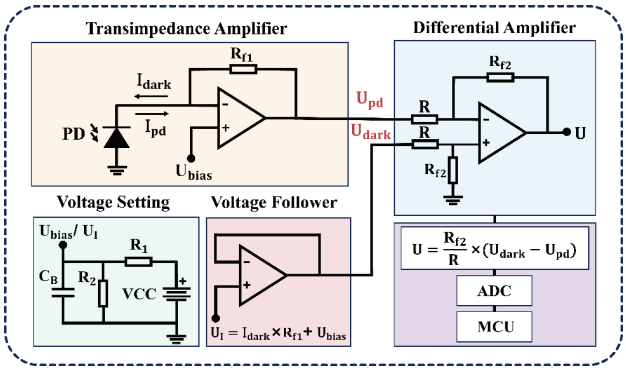

Figure 6: The hardware schematic of the detection circuit.

for analyzing multi-component absorption from mixed spectra and accurately identifying concentrations.

3.1 Accurate and Reliable Sensing System Design

In this section, starting with the NIR absorption characteristics of substances, we develop an affordable and lightweight optical sensing system. By optimizing the circuit design, we enhance the system's sensitivity and accuracy, and implement a series of measures to reduce the primary interference from water absorption.

3.1.1 Urine sensing model and system. In this section, we first model the relationship between NIR light and urine composition and then build the sensing system on this basis.

Urine sensing principle. Quantum mechanics allows us to quantify vibrational energy[28, 29], which can be expressed as:

$$E_v = (n + \frac{1}{2})h\nu_v, \tag{1}$$

where n is the vibrational quantum number, h is Planck's constant, and ν_v is the molecular vibrational frequency. Molecules need meet certain conditions to absorb NIR radiation, namely, the energy of the radiation photon ($E_{photon} = h\nu$) must precisely match the energy difference between one vibrational energy level and another. Assuming a molecule transitions from vibrational level n to n' (where $n' > n$), according to Eq.(1) the energy difference ΔE should be:

$$\Delta E = E_{v'} - E_v = (n' + \frac{1}{2})h\nu_v - (n + \frac{1}{2})h\nu_v = (n' - n)h\nu_v. \tag{2}$$

That is, in order for the transition to occur, the frequency ν of the radiated light must satisfy: $\nu = (n' - n)\nu_v$. Transitions to higher quantum numbers generate overtone peaks (such as from $n = 0$ to $n' = 2$, etc.), and additionally, combination bands arise from the interaction of multiple vibrational modes[30]. This is the principle behind the formation of absorption peaks in the NIR region.

We used a UV-Vis-NIR spectrophotometer to analyze the NIR light absorption of three substances, as depicted in Fig. 2. The data revealed spurious peaks at higher wavelengths and weak absorption at lower wavelengths, leading us to focus on the mid-band range of 1000-2000 *nm*, where we identified unique characteristic peaks of each substance, shown in Fig. 3. Additionally, NIR spectra typically feature broad frequency peaks and overlapping spectral features, complicating our analysis. We also observed, as shown in Fig.4, that water exhibits a strong absorption peak centered at 1500 *nm*, with which the absorption peaks of albumin (ALB) and glucose (GLU), both containing O-H bonds, significantly overlap. This overlap nearly completely masks their characteristic absorption, prompting us to investigate other hydrogen-containing groups to enhance our concentration determination capabilities.

Sensing System Design. Based on the sensing principles described previously, we developed a system that utilizes five LEDs to cover all characteristic wavelengths, with their spectral distribution shown in Fig. 5. By sequentially activating these LEDs, we can measure the absorption intensity at various wavelengths. Compared to traditional spectrometers that use mixed light sources and diffraction gratings, our system is simpler and more cost-effective. Correspondingly, we use InGaAs photodiodes with a responsivity range of 800-2200 *nm* at the detection end to receive light signals and perform photoelectric conversion.

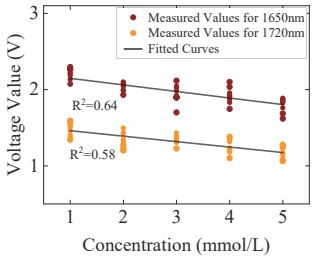

Figure 7: Concentration Response of UA at Multiple Wavelengths.

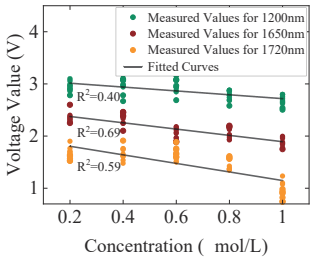

Figure 8: Concentration Response of ALB at Multiple Wavelengths.

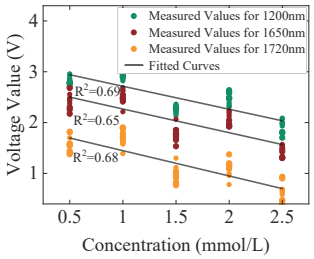

Figure 9: Concentration Response of GLU at Multiple Wavelengths.

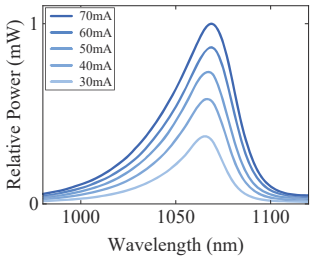

Figure 10: Spectral Power of LED at Various Currents.

Due to the low emission intensity of LEDs, we optimise the detection circuit design to enhance our system's sensitivity and accuracy. First, we apply a reverse bias voltage to the photodiode to operate it in photoconductive mode, which enhances its photosensitivity. However, the small photosensitive area of the photodiode captures only weak light intensity, presenting challenges in detecting subtle changes caused by light absorption. Therefore, we designed a two-stage amplification circuit: the first stage employs transimpedance amplification to enhance the photodiode current under reverse bias, and the second stage performs differential amplification, further boosting the difference between the real-time current and the dark current under identical conditions and amplification factors. This design enables us to precisely capture minute changes in the photocurrent. The hardware schematic of this detection circuit is illustrated in Fig. 6. Finally, the analog-to-digital converter (ADC) precisely samples the light absorption values, which are then transmitted to the MCU for further processing.

3.1.2 Spectral calibration to remove water interference. Although we have avoided the water absorption peaks, it still exhibits strong absorption in the NIR region, which also affects our observation of other characteristic peaks. Particularly, due to the additive nature of absorption, the measured values actually reflect the total absorption of both water and other components. To resolve this, we use the spectrum of pure water as a baseline to calibrate the spectrum of the mixed solution.

According to Beer's law[31] the total absorption at wavelength λ is:

$$A(\lambda) = -log_{10}^{\frac{I_t(\lambda)}{I_0(\lambda)}} = \varepsilon_x(\lambda)c_x l + \varepsilon_w(\lambda)c_w l, \tag{3}$$

where $I_t(\lambda)$ and $I_0(\lambda)$ are the transmitted and incident light intensities. $\varepsilon_x(\lambda)$ and $\varepsilon_w(\lambda)$ are the molar absorptivities of substance x and H_2O at wavelength λ, respectively. c_x and c_w are the concentrations of substance x and H_2O, respectively. l is the optical path length. The absorption of pure water at wavelength λ is:

$$A_w(\lambda) = -log_{10}^{\frac{I_t^w(\lambda)}{I_0^w(\lambda)}} = \varepsilon_w(\lambda)c_w l. \tag{4}$$

By subtracting the water absorption $A_w(\lambda)$ directly from the mixed solution's absorption $A(\lambda)$, we obtain the net absorption due to substance x, expressed as:

$$c_x = \frac{1}{\varepsilon_x l}\left[A(\lambda) - A_w(\lambda)\right] = \frac{1}{\varepsilon_x l} log_{10}^{\frac{I_t^w(\lambda)}{I_t(\lambda)}}. \tag{5}$$

It's important to note that $A(\lambda)$ in the Lambert-Beer's Law is a dimensionless quantity, so we can consider $I_t(\lambda)$ as the photocurrent generated by the light intensity converted by the photodiode.

3.2 Multi-dimensional Spectral Information Recovery

3.2.1 Limitations. Currently, our sensing system provides light absorption values of several LEDs, but its resolution is significantly lower compared to a spectrometer capable of achieving a few nanometers resolution. Specifically, LEDs typically emit light with a Gaussian-like distribution centered on their peak wavelength, resulting in wide emission bands, and photodiodes are unable to selectively detect specific wavelengths of light. Due to these performance limitations, our system currently achieves a spectral resolution of about 100 *nm*, meaning it can only obtain a few discrete absorption points rather than a continuous spectrum.

We conducted experiments attempting to identify different concentrations using only a few response values obtained from LED light sources, and selected LEDs whose peak wavelengths correspond as closely as possible to the absorption peaks. For each substance, we conducted ten experiments at five different concentrations and fitted the relationship of absorption values at these concentrations. The results, as shown in Fig. 7, Fig. 8 and Fig. 9, reveal that the coefficient of determination (R^2) for all fits is below 0.7. This demonstrates that relying solely on light absorption values from a few LEDs to determine the concentration of substances is unreliable.

There are several problems with this method: (i) Assuming absorption across the entire broadband as absorption at the peak wavelength may lead to erroneous results; (ii) The peak wavelength does not necessarily coincide with the characteristic wavelength of interest; (iii) NIR spectroscopy exhibits broad, overlapping spectral peaks, making substance analysis inaccurate when reduced to a single value. Therefore, it is very difficult for us to obtain spectral information using such a simple and limited-performance system.

3.2.2 Rationale of spectral recovery. Typical spectroscopy system choices use expensive dispersive elements, extremely narrow laser emission sources, or complex detectors. These designs add significantly to the cost and makes the system bulky, contradicting our goal of a low-cost design. And there are also some research that directly use these absorption values for identification, but we have demonstrated their limitations in urine testing.

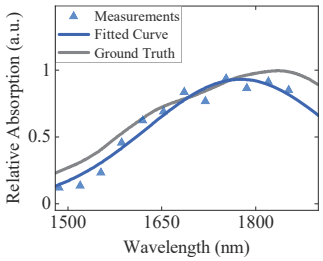

Figure 11: Spectral fitting performance of UA.

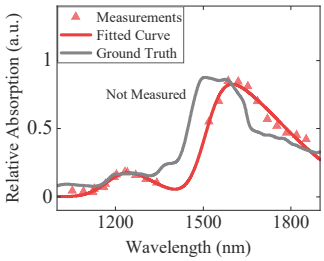

Figure 12: Spectral fitting performance of ALB.

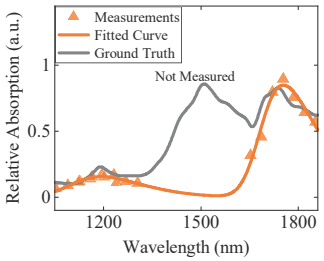

Figure 13: Spectral fitting performance of GLU.

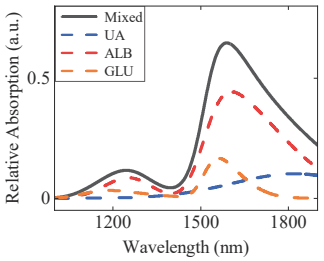

Figure 14: Mixed spectral decomposition.

Fortunately, by parsing the photodiode response, we found that fine-grained information could be recovered from it. It is known that photodiodes have different sensitivities to different wavelengths of light and perform photoelectric conversion. That is, when receiving mixed light over a wide spectral range, although the photodiode only outputs one single value, it actually contains information within the entire spectrum range. This observation means that we have the opportunity to recover multi-dimensional spectra from the single output of the photodiode. The detailed analysis process is as follows.

The response I of a photodiode can be expressed as:

$$I = \int P_{pd}(\lambda)T(\lambda)S(\lambda)\,\mathrm{d}\lambda = \int K(\lambda)T(\lambda)\,\mathrm{d}\lambda, \tag{6}$$

where $P_{pd}(\lambda)$ is the intensity of light emitted by the light source and reaches the photodiode without any loss through media other than air, $T(\lambda)$ is the light transmittance, and $S(\lambda)$ is the spectral sensitivity of the photodiode. $P_{pd}(\lambda)$ and $S(\lambda)$ are known, and we denote them as constant coefficients $K(\lambda)$. The relationship between I and the voltage U we obtained can be expressed as:

$$U = \frac{R_{f2}}{R}(U_{dark} - U_{pd}) = \frac{R_{f1}R_{f2}}{R}(I_{dark} - I_{pd}) = \frac{R_{f1}R_{f2}}{R}I, \tag{7}$$

where the meaning of each of these electrical attributes is illustrated in the circuit diagram of Fig. 6. As previously mentioned, the law of light absorption dictates that the relationship between absorption and transmittance can be expressed as:

$$A = lg\frac{I_0}{I_t} = -lgT, \tag{8}$$

where A and T is the spectral absorbance and transmission values, respectively. It can be seen that A and T are interconvertible, so our goal is to express the substance's absorption of light by solving for $T(\lambda)$ from Eq. (6). Suppose we discretise I as a sum of the response values at n wavelengths, then Eq. (6) can be expressed as:

$$\widetilde{I} = \sum_{i=1}^{n} K(\lambda_i)T(\lambda_i). \tag{9}$$

And if we can obtain response values of m dimensions within the spectral range, Eq. (9) can be expressed in matrix form as:

$$\begin{pmatrix} K_{11} & K_{12} & \cdots & K_{1n} \\ K_{21} & K_{22} & \cdots & K_{2n} \\ \vdots & \vdots & \ddots & \vdots \\ K_{m1} & K_{m2} & \cdots & K_{mn} \end{pmatrix} \begin{pmatrix} T_1 \\ T_2 \\ \vdots \\ T_n \end{pmatrix} = \begin{pmatrix} I_1 \\ I_2 \\ \vdots \\ I_m \end{pmatrix} \leftrightarrow K \cdot T = \widetilde{I}, \tag{10}$$

where $\widetilde{I}$ is the m-dimensional column vector of responses, K is the coefficient matrix of $m \times n$ dimension, and T is the n-dimensional column vector of unknowns. According to the rules for solving matrices, we can successfully solve for the vector T when $m \geq n$. This also means that the more response values obtained then the higher the resolution of the spectrum.

3.2.3 Implementation of spectral recovery. In order to obtain light response values in different dimensions, we need to use the existing LED array to obtain different light emission spectra. First, we know that the luminous efficiency of LEDs can be adjusted by the drive current, so we measured the spectra of LEDs at different currents using a spectrometer, and the results are shown in Fig. 10. It can be seen that there is a linear relationship between the luminous intensity and the drive current, and the power of the LED at different currents can be converted through an approximate proportional coefficient. This means that the response values obtained by LEDs at different operating currents belong to the same dimension, making it impossible to solve for I in Eq. 10.

Furthermore, since expanding only the current dimension doesn't provide a solution, we considered simultaneously increasing the number of LEDs. By combining the emission spectra of two adjacent LEDs at multiple currents, we can easily obtain multiple desired response values in different dimensions. To clarify, let's assume X_i denotes the operating current i of a particular LED. Then the set of all valid current combinations for two LEDs can be expressed as:

$$S = \bigcup_{k=0}^{n} \left\{ A_i B_j : i, j \in \{0, 1, \ldots, n\} \wedge (i \neq j \vee i = j = k) \right\}. \tag{11}$$

Based on the principles, increasing m improves the accuracy of spectrum recovery, and m depends on the size of n. However, as m increases, the time cost for detection also rises. Also, if n is too large, the similarity of the combined LED waveforms increases, making it difficult to achieve an effective solution. Therefore, after balancing time and efficiency, we ultimately chose $n = 3$.

Additionally, another problem is that spectrometers provide only the relative power spectrum, leaving us unaware of the exact power the LED emits in each operating state. Moreover, the radiant power is not the same as $P_{pd}(\lambda)$ in Eq. (6), so we need to perform some calculations. First of all, the total radiant power, P_e, of an LED in any operating state (assumed to be U_e and I_e) can be calculated from the known photoelectric conversion efficiency, η, using the formula $P_e = \eta \times U_e I_e$. Next, knowing P_e and the relative power

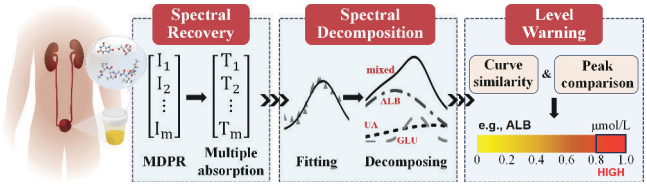

Figure 15: The concentration prediction process of UrineSpec.

spectrum obtained from a spectrometer, we can easily calculate the radiant power at each wavelength, $P_e(\lambda)$. Finally, applying the Inverse Square Law[32], the optical power density I_r received by the photodiode is $I_r = \frac{P_e}{4\pi d^2}$, where d is the distance from the LED to the photodiode. d is calculated using the formula $d = l/cos\alpha$, where l is the distance between the emission and detection planes, and α is the elevation angle of each LED to the photodiode. Then $P_{pd}(\lambda)$ is derived using $P_{pd}(\lambda) = I_r \times \pi r^2$, with r as the sensitivity radius of the photodiode.

Finally, we met all the requirements for solving Eq.10. In the solving process, we used the least squares method, minimizing the sum of squared errors to solve the matrix equation. This allowed us to find the best fit solution even in the presence of data errors. After solving for absorption at multiple wavelengths, we performed spectral fitting and tried various nonlinear fitting methods. Polynomial fitting resulted in significant peak shifts and shape differences, while Gaussian fitting was inaccurate due to the strong asymmetry of the spectra. Ultimately, we chose a skewed Gaussian function model, which aligns with the asymmetric Gaussian distribution characteristics of the spectra and allows for fixing peak positions based on the features of each absorption peak to improve fitting accuracy. Fig. 11, Fig. 12 ,and Fig. 13 shows the spectral fitting results for UA, ALB, and GLU at a certain concentration after eliminating water interference. Since ALB and GLU each have an absorption peak at both high and low wavelengths, we defined two peak positions during the fitting process. The unobserved region in the middle does not affect our detection of the dual peaks. It is evident that due to various errors present in the analysis process and sensitivity limitations, it is challenging to accurately recovery the standard spectra. However, we can still recover absorption spectra with peak characteristics and demonstrate their ability to distinguish different concentration levels in subsequent experiments.

3.3 Urine Concentration Sensing

In this section, we provide a detailed explanation of how to parse the individual absorption of substances from mixed spectroscopy and how to determine the concentration of substances based on the spectra.

Spectral deconvolution. In practical applications, the spectral data we obtain is often a result of multiple substances being mixed. Specifically, both ALB and GLU exhibit absorption due to N-H bond vibrations, leading to significant overlap in their absorption regions. Therefore, it is necessary to separate the absorption spectra of each component from the complex mixed spectrum. We have already established methods for fitting the absorption spectra of each substance and, based on these methods, developed standard curve models for each substance, making the analysis relatively straightforward. We represent the mixed spectrum as a superposition of

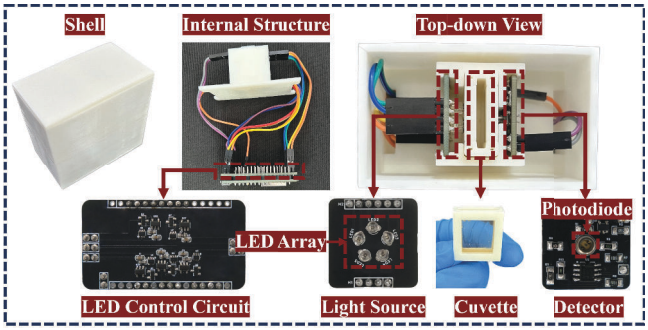

Figure 16: The prototype of UrineSpec.

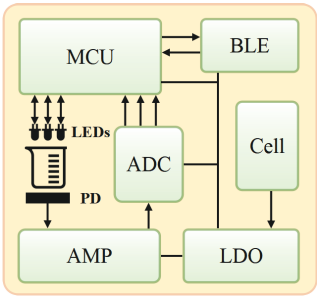

Figure 17: Absorption characteristics of water.

Figure 18: The spectral distribution of UrineSpec.

multiple skewed Gaussian functions. By initially estimating the parameter values and subsequently using the least squares method to optimize these parameters, we achieve a fit that matches the experimental data. Fig.14 illustrates an example of our analysis of the mixed spectrum.

Concentration identification. After obtaining the absorption spectrum, to ensure accurate identification, we consider both the shape and peak characteristics. First, we use Principal Component Analysis (PCA) to calculate the similarity between the unknown concentration curve and all standard concentration curves, selecting the two curves with the highest similarity as candidates. Then, we calculate the Euclidean distance between the peak absorption of the unknown concentration curve and the peak absorption of these two candidate curves, choosing the curve with the smaller distance to determine the concentration. This method effectively improves the accuracy of identification.

In summary, the concentration estimation process for a specific component using UrineSpec is shown in Fig. 15.

4 IMPLEMENT

We designed and implemented the prototype using off-the-shelf hardware components, as shown in Fig. 16. The prototype mainly includes two aspects: structural design and hardware design.

Structural design. The prototype's shell is 3D printed using opaque polylactic acid (PLA), measuring 6.8×4.0×6.3 *cm* effectively preventing external light interference. At the center is a cuvette made with opaque PLA sides and transparent glass, housing LEDs and photodiodes for optimal NIR light transmission through urine samples. The hardware circuit board lies at the bottom, featuring two parallel boards (5.1 × 2.8) *cm* connected by pins. The upper

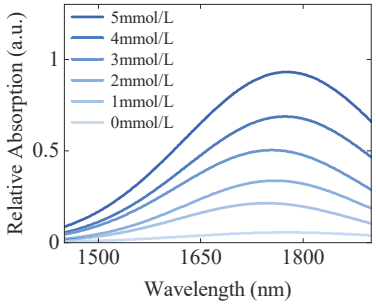

(a) UA concentration spectra.

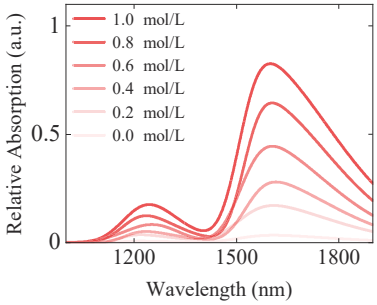

(a) ALB concentration spectra.

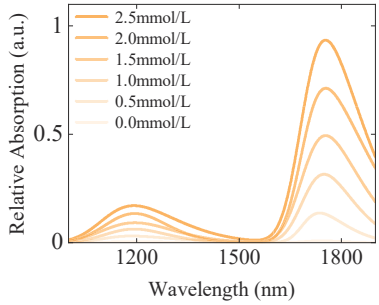

(a) GLU concentration spectra.

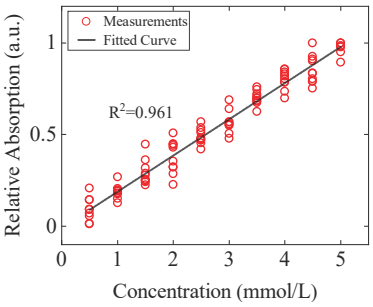

(b) Peak absorption vs. concentration.

Figure 19: Sensing Performance of uric acid (UA).

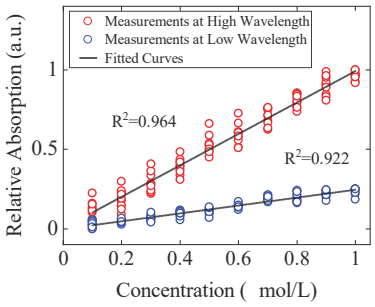

(b) Peak absorption vs. concentration.

Figure 20: Sensing Performance of albumin (ALB).

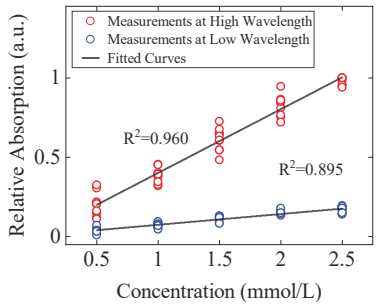

(b) Peak absorption vs. concentration.

Figure 21: Sensing Performance of glucose (GLU).

layer contains the optical sensing and power units, while the lower layer uses an ESP32 for computational and transmission functions, suitable for low-power sensing applications.

Hardware design. The hardware consists of three main components: the optical sensing unit, the power unit, and the computational unit. The optical sensing unit includes NIR-LEDs with peak wavelengths of 1070 *nm* (MTE7110C1), 1200 *nm* (MTE1201C1), 1300 *nm* (MTE1301C1), 1650 *nm* (MTE5116C1), and 1720 *nm* (MTE2117C1). and a photodiode (LSIPD22 -0.5) with a photosensitivity range of 800 to 2200 *nm*. A constant-current driver chip (QX7138) ensures stable LED luminous power, and the OPA328 amplifier provides high-frequency transimpedance gain. The computational unit, controlled by an ESP32, manages the LEDs, samples voltage values, and transmits data via Bluetooth. The power unit uses lithium batteries, providing a stable 3.3V output through a Low Dropout Regulator (LDO) to ensure reliable power for the system. The hardware consists of three main components including the optical sensing unit, the power unit,and the computational unit. The logical relationship between the modules is shown in Fig. 17. Our experimental setup in a real-world scenario is shown in Fig. 18.

5 EVALUATION

In this section, we first perform benchmark experiments to evaluate our spectral recovery algorithm and feature extraction methods. Next, we conduct experiments to assess the sensing performance of UrineSpec, focusing on sensitivity and stability. Following this, we evaluate the overall sensing accuracy evaluation and conduct robustness experiments considering multiple factors. Finally, we present a case study to demonstrate the feasibility of real-world urine sensing.

5.1 Performance of Sensing

5.1.1 Sensing Performance of Single Substance. We conduct experiments to understand the sensing performance of the UrineSpec for UA, ALB, and GLU. Specifically, we examined the sensitivity of the sensing system by performing 10 sets of experiments for each substance. Sensitivity indicates how finer concentrations are perceived.

Sensing urea acid. For uric acid(UA), we tested 11 concentration levels, ranging from 0 $mmol/L$ to 5 $mmol/L$, with increments of 0.5 $mmol/L$. This setup is based on the normal range of uric acid levels in human urine, which is between 1.49 and 4.46 $mmol/L$. In the experiment, we prepare artificial urine by adding certain concentrations of substances to deionized water to simulate real urine. Please note that unless otherwise specified, the artificial urine mentioned later is prepared using this method. Specifically, we dissolve 25 g of urea, 9 g of sodium chloride, 1.5 g of potassium chloride, 2.5 g of sodium dihydrogen phosphate, and 0.6 g of sodium citrate in 1 L of deionized water. The specific process for a solution of UA at a certain concentration is as follows: we first prepared a high-concentration uric acid solution of 1 mol/L. Using 50 mL

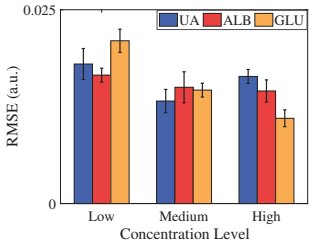

Figure 22: Decomposition error of mixed spectrum.

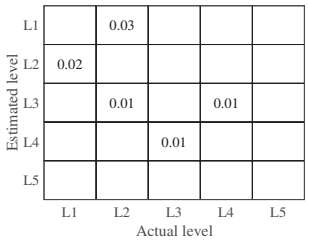

Figure 23: The accuracy of sensing UA.

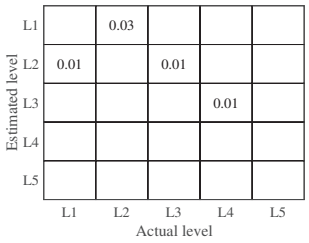

Figure 24: The accuracy of sensing ALB.

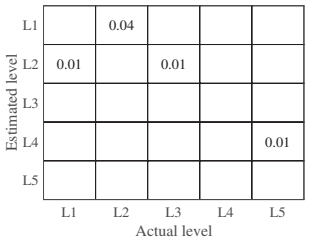

Figure 25: The accuracy of sensing GLU.

of artificial urine as the base fluid, we added 25 μL of the high-concentration uric acid solution each time, increasing the uric acid concentration by 0.5 $mmol/L$. This process produced a uric acid solution with a concentration of 0.5 $mmol/L$, and so forth.

Fig. 19(a) shows the absorption spectra fitted at different concentrations with 1 $mmol/L$ intervals. It can be observed that the peak wavelengths of different concentrations are slightly different but are generally around 1760 nm. Additionally, the shapes of the spectra are similar across concentrations, but the absorption values vary significantly. This implies that concentration can be differentiated based on the shape and peak features of the spectrum. In Fig. 19(b), the circles represent the measurement values from 10 groups, and the black line represents the fitted curve. The relationship between peak absorption and uric acid concentration exhibits a strong linearity, with an R^2 value of 0.96, indicating high model accuracy.

Sensing albumin. To detect urine protein levels, we used albumin (ALB), the primary protein in urine. The experiment was designed with a concentration range from 0 to 1 $\mu mol/L$, with a step size of 0.1 $\mu mol/L$, for a total of 11 concentration levels. This is because an ALB concentration in urine between 0.3-0.6 $\mu mol/L$ is a critical threshold, and repeatedly exceeding this value may indicate kidney problems. The specific procedure is as follows: we first prepared a high-concentration albumin solution of 0.2 $mmol/L$. Using 20 mL of artificial urine as the base fluid, we added 10 μL of the high-concentration albumin solution each time, increasing the albumin concentration by 0.1 $\mu mol/L$. Fig. 20(a)shows the absorption spectra fitted at different concentrations with 0.2 $\mu mol/L$ intervals. Fig. 20(b) presents the peak absorption at high and low characteristic wavelengths across various ALB concentrations, with black dots representing measurements from 10 groups and the black line indicating the fitted curve. It is evident that there is a strong linear relationship between the absorption values at both characteristic peaks and protein concentration, with both exhibiting a goodness of fit of $R^2 = 0.96$, demonstrating robust linearity.

Sensing glucose. For glucose (GLU), we assessed five concentration levels from 0.5 $mmol/L$ to 2.5 $mmol/L$, with a step size of 0.5 $mmol/L$. These concentrations cover the medical requirements for detecting different levels of GLU in urine. The specific procedure is as follows: we first prepared a high-concentration glucose solution of 1 mol/L. Using 40 mL of artificial urine as the base fluid, we added 20 μL of the high-concentration albumin solution each time, increasing the albumin concentration by 0.5 $mmol/L$. Fig. 21(a) depict the absorption spectra curves at 0.5 $mmol/L$ intervals in low and high characteristic wavelength areas. Fig. 21(b) illustrates the peak absorption at both high and low characteristic wavelengths for varying GLU concentrations, with black dots representing data from 10 groups and the black line showing the fitted curve. A strong linear relationship is evident between the absorption values at both characteristic peaks and glucose concentration, with both showing a goodness of fit of $R^2 = 0.9$, demonstrating robust linearity.

5.1.2 Sensing Performance of Multi-component Solutions. In this experiment, to demonstrate effective distinction of each substance's concentration in mixed solutions, we selectively design experiments using combinations of low, medium, and high concentrations for each substance. This approach covers all possible concentration variations without the need to test an extensive number of combinations. Specifically, the low, medium, and high concentrations for the three substances are: uric acid (1, 3, 5 $mmol/L$), protein (0.1, 0.5, 0.9 $\mu mol/L$), and glucose (0.5, 1.5, 2.5 $mmol/L$).

We measured the mixed absorption spectra of all combinations and resolved the individual absorption spectra of the three substances from these mixtures. For each concentration of the mixture, we conducted ten experiments and used the Root Mean Square Error (RMSE) to quantify the deviation between the resolved spectra and the standard spectra of each individual substance. The results are presented in Fig. 22, showing minimal errors with an average value of approximately 0.015. This indicates that the absorption spectra of the substances can be accurately resolved from the mixed solutions. By basing our analysis on individual spectra, we can achieve the recognition granularity for each substance as described in Section 5.1.1.

5.2 Urine Sensing Accuracy

We assessed the precision of the UrineSpec in differentiating between five concentration levels of urea acid (UA), albumin (ALB) and glucose (GLU). The five levels are shown in Table. 1, except for ALB concentration which is in $\mu mol/L$, all other concentration units are in $mmol/L$. These five levels are sufficient for early warning purposes, and only three levels (normal, below normal, above normal) are generally required for medical purposes.

The preparation process for each substance's concentration solutions is the same as described in Section 5.1. For each concentration level of each substance, we conducted 100 estimations. The results for UA, ALB, and GLU are shown in Fig. 23, Fig. 24 and Fig. 25

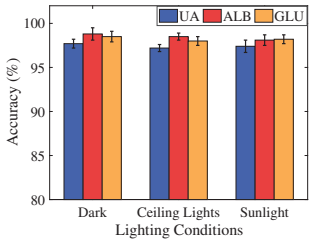

Figure 26: Performance in different light environments.

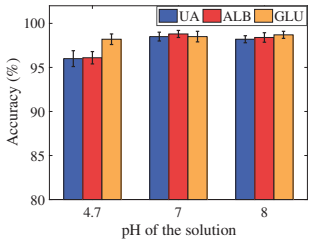

Figure 27: Performance at different urine pH levels.

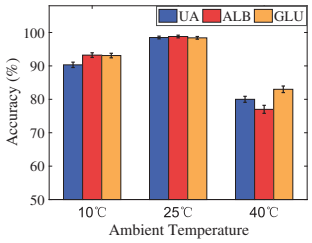

Figure 28: Performance at different temperatures.

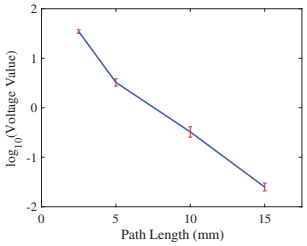

Figure 29: Photodiode's response under different light paths.

Table 1: Concentration levels for testing accuracy.

	L1	L2	L3	L4	L5
Uric acid (UA)	0-1	1-2	2-3	3-4	4-5
Albumin (ALB)	0-0.2	0.2-0.4	0.4-0.6	0.6-0.8	0.8-1
Glucose (GLU)	0-0.5	0.5-1	1-1.5	1.5-2	2-2.5

respectively. The findings are as follows: (i) For UA solutions within the 0-5 $mmol/L$ range at five concentration levels, the average recognition accuracy of UrineSpec is 98.4% with a resolution of 0.5 $mmol/L$. (ii) For protein solutions within the 0-1 $\mu mol/L$ range at five concentration levels, the average recognition accuracy of UrineSpec is 98.8% with a resolution of 0.1 $\mu mol/L$. (iii) For glucose solutions within the 0-2.5 $mmol/L$ range at five concentration levels, the average recognition accuracy of UrineSpec is 98.6% with a resolution of 0.25 $mmol/L$.

In addition, the results show that at low concentrations, the differences between the spectral curves of different concentrations are relatively minor, and the peaks are not distinct, increasing the likelihood of misjudgment. At higher concentrations, the absorption is stronger and the peak features are more prominent, leading to higher detection accuracy. Overall, the average detection accuracy of UrineSpec for the three substances across five concentration levels is 98.6%.

5.3 Performance under Different Parameters

5.3.1 Performance in different light environments. To evaluate the performance of UrineSpec under different lighting conditions, we conducted experiments in three typical environments: darkness, sunlight, and indoor ceiling light. The experimental results in Fig. 26 show that UrineSpec's prototype could adapt to various types of ambient light with a mean accuracy of 98%. The excellent resistance to light interference is primarily due to the use of opaque materials to encase the entire light-sensing system. Additionally, the detectors employed are sensitive to specific near-infrared wavelengths.

5.3.2 Performance at different urine pH levels. Urine pH typically fluctuates between 4.5 and 8.0 due to dietary influences. To study the recognition accuracy under different pH conditions, we conducted experiments with pH values of 4.7 (acidic), 7 (neutral), and 8 (alkaline). As shown in Fig. 27, the results indicate that in an acidic environment, the recognition accuracy of UA decreases with significant error, possibly due to reduced solubility in acidic conditions. ALB shows decreased recognition accuracy due to denaturation and structural changes affecting its absorption properties in an acidic conditions. In contrast, glucose maintains stable recognition accuracy, indicating that its molecular structure and absorption characteristics are not significantly affected by varying pH levels. To enable our system to adapt to different pH environments, we can add pH sensing functionality and establish standard curves under various conditions for calibration.

5.3.3 Performance at different temperatures. Temperature variations significantly impact optoelectronic devices, especially photodiodes. Most notably, an increase in temperature leads to a significant rise in the dark current of photodiodes. Since we use a differential circuit to amplify the generated photocurrent rather than the changes in dark current, the resulting impact is almost eliminated. Nevertheless, the changes in Photoelectric Conversion Efficiency (PCE) and photoresponse rate due to temperature fluctuations cannot be ignored. Therefore, we investigated the perception accuracy of UrineSpec at three different ambient temperatures: 10°C, 25°C (room temperature), and 40°C.

The results are shown in Fig. 28. At low temperatures, the accuracy slightly decreases due to an increase in the photodiode's PCE and faster response speed. The impact of high temperatures is the most significant, leading to a decrease in the photodiode's PCE and slower response speed, with these changes being more pronounced compared to low temperatures. Additionally, increased noise further contributes to a substantial reduction in accuracy. Overall, variations in the photodiode's response characteristics have caused significant errors in our analysis of feature absorption derived from the photodiode's response. To mitigate the effects of temperature, professional instruments can be used to measure the photodiode's response at different temperatures, and temperature-sensitive components can be added to calibrate errors in real-time.

5.3.4 The impact of optical path lengths. The selection of the optical path length primarily considers the absorption characteristics of the substance. A longer optical path results in excessive attenuation of light, while a shorter optical path makes the absorption characteristics of the substance being measured less pronounced. To determine the optimal path length, we varied the optical path length and measured the photodiode's response under a constant light intensity, using an amplifier with the highest possible gain and output amplitude. Fig. 29 shows the measurement results. The intensity decreases exponentially with increasing path length, and

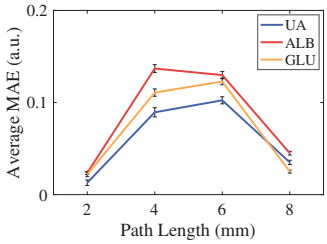

Figure 30: Performance in different light environments.

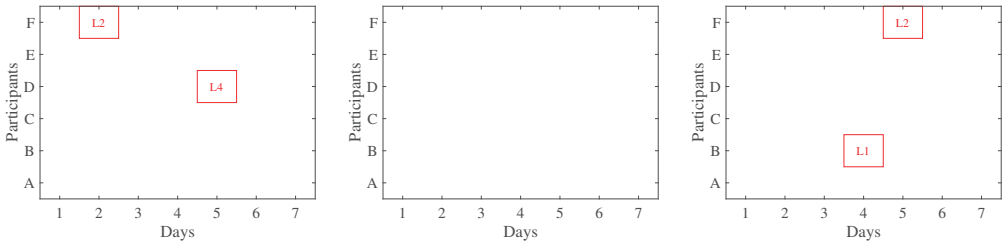

(a) UA (b) ALB (c) GLU

Figure 31: Concentration warning results for the three substances in the case study.

when the path length exceeds 1 *cm*, the light intensity has nearly completely decayed.

Based on the effective detection of light intensity, we further studied the average Mean Absolute Error (MAE) of the fitted concentration curves under different optical path lengths. The results in Fig. 30 show that at optical path lengths of 4 *mm* and 6 *mm*, the differences between the concentration curves are more pronounced, facilitating accurate concentration identification. Therefore, we ultimately selected an optical path length of 5 *mm* for our experiments.

5.4 Case Study

In this case study, we aim to evaluate the performance of UrineSpec for level alerting in real scenarios by estimating the concentrations of UA, ALB, and GLU in actual human urine. We conducted morning urine tests on six volunteers over a continuous seven-day period, taking into account the distribution of gender and age. Among these participants, the three female volunteers were aged 23, 37, and 55, and the three male volunteers were aged 25, 48, and 65, labeled A to F. They were all healthy individuals. To simulate disease conditions, we added three substances to the volunteers' urine to prepare spiked samples.

Fig. 31 shows the detection results for the three substances, with the incorrectly predicted results marked by red boxes. As can be seen, we randomly assigned concentration levels for each substance to each participant, ensuring all levels were covered. The overall accuracy was 96.8%, with errors mainly occurring between adjacent levels and no significant bias. For example, on the second day for Participant F, the UA level was incorrectly estimated from L1 to L2. The high accuracy across different substances and days demonstrates the robustness and reliability of the UrineSpec system. Furthermore, the consistent performance across various participants highlights the system's stability and potential for widespread application in diverse populations. Overall, the case study validates the effectiveness of the UrineSpec in real-world urinalysis and highlights the importance of dietary adjustments or timely professional medical examination if substance levels persistently fall outside the normal range.

6 RELATED WORKS

In this section, we review existing works related to urine detection and light sensing.

Urine Detection The traditional method for diagnosing chemical constituents in urine relies on test strips[33, 34] or dry chemical analysis[35, 36] as well as non-invasive sensors[37–40]. For instance, Penders[41] demonstrated an automated urine test strip reading system, while Simith[42] proposed a "lab on a chip" dipstick reader that can be used in conjunction with smartphones. Teekayupak et al.[13] reported an electrochemical sensor platform using modified cotton fibers for non-enzymatic UA detection and J.P et al.[14] created a non-enzymatic sensor based on zirconium copper oxide microflowers (Zr/CuO MF) for GLU detection in various bodily fluids. However, these analyzers are hindered by their high costs, instability, and inability to support continuous monitoring, which limits their practical applications. New IoT-driven liquid detection methods harness the potential of smartphones to identify urine components by measuring properties such as viscosity and acoustic impedance[15, 16]. For example, Akte-Liquid[15] identifies serum albumin based on acoustic impedance, and Vi-Liquid[17] uses a smartphone to measure viscosity and detect substances like sodium urate and ovalbumin. However, these methods are limited toidentifying single components and are ineffective for analyzing complex real urine mixtures.

Light Perception. Existing lightweight optical sensing solutions enable applications such as human sensing[43], hand pose reconstruction[44], and gesture recognition[45, 46] by leveraging light transmission characteristics. More detailed innovative perception research includes ultra-low power gaze tracking[47], battery-free eye trackers[48], non-invasive glucose monitoring[49], and real-time bilirubin measurement[50]. Low-cost optical absorption detection methods include Smart-U[51] for food identification, AI-light[52] for detecting alcohol concentration in beverages, and NIRSCam[53] for estimating food calories. However, they are limited to using coarse LED light absorption values for imprecise identification. Furthermore, Jiang et al.[54] devised a mobile device with a NIR spectroscopy scanner for sugar content identification in beverages. Lili[55] employs LEDs and a photodiode to detect liquor absorption spectrum, aiding in assessing liquor quality during fermentation. However, they are only capable of identifying single substances or conducting qualitative analysis. UrineSpec offers quantitative analysis of multiple urine constituents, and our system excels in capturing fine-grained spectral data and identifying multiple components, outperforming others in detecting weak urine constituents.

7 DISCUSSION

Comparison with alternative methods. We compare UrineSpec with existing urine testing methods, including the portable urine chemistry analyzer for continuous home monitoring, and the advanced fully automated analyzer for medical use. The results are shown in Table. 2. UrineSpec is cost-effective at $100 and requires no consumables, ideal for household use. It provides semi-quantitative accuracy across five levels. While it measures fewer indicators, UrineSpec efficiently targets essential metrics, offering a practical alternative to traditional analyzers.

Table 2: Comparison of urine testing methods.

Feature	Fully Auto Analyzer	Chemistry Analyzer	**UrineSpec**
Cost	$5,000+	$300	**$100**
Consumables	Yes	Yes	**No**
Accuracy	Quantitative	Semi-quant. (Neg/Pos)	**Semi-quant. (5 Levels)**
Indicators	11+	14	**3**
Use Case	Medical	Household	**Household**

Extending to other potential applications. UrineSpec detects concentration levels through the unique near-infrared absorption of biomacromolecules. This means our system can also detect other biomarkers that exhibit distinctive and significant absorption in the near-infrared spectrum. Additionally, our design can be adapted to other wavelength regions. With appropriate light sources and detectors for specific absorption wavelengths, detection in these regions is feasible. Therefore, we can further explore the detection of other physiological indicators in urine and other bodily fluids, which is also our ongoing work.

Remaining challenges. We believe that the following challenges remain: (1) Commercially available NIR LEDs are quite limited, as they typically emit at fixed wavelengths, preventing full spectral coverage. Additionally, their intensity is relatively low, making it difficult to penetrate highly turbid liquids, thus limiting the scope of detectable samples. (2) Detecting multiple substances in a mixture could be a challenge. In principle, as long as a substance exhibits NIR absorption, its concentration can be detected. However, due to overlapping absorption peaks in the NIR spectrum, it may not be very accurate to decompose the mixed spectrum and extract the absorption profiles of each individual substance.

8 CONCLUSION

In this work, we present the design, implementation and evaluation of UrineSpec, a lightweight system that can detection of macromolecular substances in urine. Through both theoretical analysis and experiment evaluation, we demonstrate the effectiveness of the UrineSpec in measurement of UA, ALB and GLU in urine. We believe that this system can provide effective physiological data support for daily chronic disease monitoring.

ACKNOWLEDGEMENTS

We appreciate the valuable comments and feedback from the anonymous reviewers and shepherd. This research was supported by the Shaanxi International Science and Technology Cooperation Program 2022KW-11 and 2024GH-ZDXM-50.

REFERENCES

[1] Abraham Joseph Pellissery, Poonam Gopika Vinayamohan, Leya Susan Viju, Divya Joseph, and Kumar Venkitanarayanan. 2023. Application of Urine Metabolomics as a Marker in Health and Disease. In *Advances and Challenges in Urine Laboratory Analysis*. IntechOpen.

[2] Cindy George, Justin B Echouffo-Tcheugui, Bernard G Jaar, Ikechi G Okpechi, and Andre P Kengne. 2022. The need for screening, early diagnosis, and prediction of chronic kidney disease in people with diabetes in low-and middle-income countries—a review of the current literature. *BMC medicine* 20, 1 (2022), 247.

[3] Sam Dagogo-Jack. 2021. Screening, monitoring, prevention, and treatment strategies for chronic kidney disease in patients with type 2 diabetes. (2021).

[4] Beatriz Sequeira-Antunes and Hugo Alexandre Ferreira. 2023. Urinary biomarkers and point-of-care urinalysis devices for early diagnosis and management of disease: a review. *Biomedicines* 11, 4 (2023), 1051.

[5] Haochen Guan, Yuqi Zheng, Xun Zhou, Ying Xu, Chensheng Fu, Jing Xiao, and Zhibin Ye. 2020. Efficacy of different urinary uric acid indicators in patients with chronic kidney disease. *BMC nephrology* 21 (2020), 1–9.

[6] Tao Yuan, Shixuan Liu, Yingyue Dong, Yong Fu, Yan Tang, and Weigang Zhao. 2020. Effects of dapagliflozin on serum and urinary uric acid levels in patients with type 2 diabetes: A prospective pilot trial. *Diabetology & Metabolic Syndrome* 12 (2020), 1–9.

[7] Marc Evans, Ruth D Lewis, Angharad R Morgan, Martin B Whyte, Wasim Hanif, Stephen C Bain, Sarah Davies, Umesh Dashora, Zaheer Yousef, Dipesh C Patel, et al. 2022. A narrative review of chronic kidney disease in clinical practice: current challenges and future perspectives. *Advances in therapy* 39, 1 (2022), 33–43.

[8] Ellen K Hoogeveen. 2022. The epidemiology of diabetic kidney disease. *Kidney and Dialysis* 2, 3 (2022), 433–442.

[9] Guillaume Résimont, Laurence Piéroni, Edith Bigot-Corbel, Etienne Cavalier, and Pierre Delanaye. 2021. Urinary strips for protein assays: easy to do but difficult to interpret! *Journal of Nephrology* 34 (2021), 411–432.

[10] Maria Stella Graziani, Giovanni Gambaro, Lucilla Mantovani, Alessandro Sorio, Tewoldemedhn Yabarek, Cataldo Abaterusso, Antonio Lupo, and Paolo Rizzotti. 2009. Diagnostic accuracy of a reagent strip for assessing urinary albumin excretion in the general population. *Nephrology Dialysis Transplantation* 24, 5 (2009), 1490–1494.

[11] Xiyu Mao, Shiyi Xu, Shanshan Zhang, Xuesong Ye, and Bo Liang. 2021. An Integrated Flexible Multi-sensing Device for Daily Urine Analysis at Home. In *2021 IEEE Sensors*. IEEE, 1–4.

[12] Tinn Hongboontry, Surada Ponwaranon, Supphakorn Sirijongdee, Chanchana Thanachayanont, and Porpin Pungetmongkol. 2021. Low-cost and portable creatinine electrochemical sensor for non-invasive chronic kidney disease monitoring. In *2021 IEEE 21st International Conference on Nanotechnology (NANO)*. IEEE, 159–162.

[13] Kanyapat Teekayupak, Nipapan Ruecha, Orawon Chailapakul, and Nadnudda Rodthongkum. 2021. Flexible cotton-AuNP thread electrode for non-enzymatic sensor of uric acid in urine. *Cellulose* 28 (2021), 10501–10515.

[14] Chandhana JP, Navaneeth Punnakkal, Suneesh Punathil Vasu, Aarathi Pradeep, Bipin G Nair, and TG Satheesh Babu. 2023. Zirconium copper oxide microflowers based non-enzymatic screen-printed electrochemical sensor for the detection of glucose in saliva, urine, and blood serum. *Microchimica Acta* 190, 10 (2023), 390.

[15] Xue Sun, Wenwen Deng, Xudong Wei, Dingyi Fang, Baochun Li, and Xiaojiang Chen. 2023. Akte-liquid: Acoustic-based liquid identification with smartphones. *ACM Transactions on Sensor Networks* 19, 1 (2023), 1–24.

[16] Shichao Yue and Dina Katabi. 2019. Liquid testing with your smartphone. In *Proceedings of the 17th Annual International Conference on Mobile Systems, Applications, and Services*. 275–286.

[17] Yongzhi Huang, Kaixin Chen, Yandao Huang, Lu Wang, and Kaishun Wu. 2021. Vi-liquid: unknown liquid identification with your smartphone vibration. In *Proceedings of the 27th Annual International Conference on Mobile Computing and Networking*. 174–187.

[18] Liqiong Chang, Xiaofeng Yang, Ruyue Liu, Guodong Xie, Fuwei Wang, and Ju Wang. 2024. FSS-Tag: High Accuracy Material Identification System Based On Frequency Selective Surface Tag. *Proceedings of the ACM on Interactive, Mobile, Wearable and Ubiquitous Technologies* 7, 4 (2024), 1–24.

[19] Celio Pasquini. 2003. Near infrared spectroscopy: fundamentals, practical aspects and analytical applications. *Journal of the Brazilian chemical society* 14 (2003), 198–219.

[20] Yukihiro Ozaki. 2012. Near-infrared spectroscopy—Its versatility in analytical chemistry. *Analytical sciences* 28, 6 (2012), 545–563.

[21] Hui Yan, Marina De Gea Neves, Isao Noda, Gonçalo M Guedes, António C Silva Ferreira, Frank Pfeifer, Xinyu Chen, and Heinz W Siesler. 2023. Handheld near-infrared spectroscopy: State-of-the-art instrumentation and applications in material identification, food authentication, and environmental investigations. *Chemosensors* 11, 5 (2023), 272.

[22] Weixin Ye, Wei Xu, Tianying Yan, Jingkun Yan, Pan Gao, and Chu Zhang. 2022. Application of near-infrared spectroscopy and hyperspectral imaging combined with machine learning algorithms for quality inspection of grape: a review. *Foods* 12, 1 (2022), 132.

[23] Patricia Iweka, Shuso Kawamura, Tomohiro Mitani, and Takashi Kawaguchi. 2023. Online near-infrared spectroscopy for the measurement of cow milk quality in an automatic milking system. *Engineering Proceedings* 56, 1 (2023), 145.

[24] Jean-Henri Lambert. 1760. *Photometria sive de mensura et gradibus luminis, colorum et umbrae.* Sumptibus viduae Eberhardi Klett, typis Christophori Petri Detleffsen.

[25] Beer. 1852. Bestimmung der Absorption des rothen Lichts in farbigen Flüssigkeiten. *Annalen der Physik* 162, 5 (1852), 78–88.

[26] Zhining Shi, Christopher WK Chow, Rolando Fabris, Jixue Liu, and Bo Jin. 2022. Applications of online UV-Vis spectrophotometer for drinking water quality monitoring and process control: a review. *Sensors* 22, 8 (2022), 2987.

[27] Murali Dadi, Mohd Yasir, M Dadi, and M Yasir. 2022. Spectroscopy and Spectrophotometry: principles and applications for colorimetric and related other analysis. *Colorimetry* 1 (2022), 81–102.

[28] Ramamurti Shankar. 2012. *Principles of quantum mechanics.* Springer Science & Business Media.

[29] Edgar Bright Wilson, John Courtney Decius, and Paul C Cross. 1980. *Molecular vibrations: the theory of infrared and Raman vibrational spectra.* Courier Corporation.

[30] Gerhard Herzberg. 1945. Molecular spectra and molecular structure. Vol. 2: Infrared and Raman spectra of polyatomic molecules. *Molecular spectra and molecular structure. Vol. 2: Infrared and Raman spectra of polyatomic molecules* (1945).

[31] Donald F Swinehart. 1962. The beer-lambert law. *Journal of chemical education* 39, 7 (1962), 333.

[32] Frank L Pedrotti, Leno M Pedrotti, and Leno S Pedrotti. 2017. *Introduction to optics.* Cambridge University Press.

[33] Varun Kavuru, Tommy Vu, Lampros Karageorge, Devasmita Choudhury, Ryan Senger, and John Robertson. 2020. Dipstick analysis of urine chemistry: benefits and limitations of dry chemistry-based assays. *Postgraduate medicine* 132, 3 (2020), 225–233.

[34] Maria Salinas, Maite López-Garrigós, Emilio Flores, Javier Lugo, Carlos Leiva-Salinas, and PRIMary Care-LABoratory (PRIMLAB) working group. 2018. Urinary albumin strip assay as a screening test to replace quantitative technology in certain conditions. *Clinical Chemistry and Laboratory Medicine (CCLM)* 57, 2 (2018), 204–209.

[35] 2008. Urinalysis: Core Curriculum 2008. *American Journal of Kidney Diseases* 51, 6 (2008), 1052–1067.

[36] Matthijs Oyaert and Joris Delanghe. 2019. Progress in automated urinalysis. *Annals of laboratory medicine* 39, 1 (2019), 15–22.

[37] Sultan Aitekenov, Abduzhappar Gaipov, and Rostislav Bukasov. 2021. Detection and quantification of proteins in human urine. *Talanta* 223 (2021), 121718.

[38] Xing Zhang, Estefanía Sucre-Rosales, Alexander Byram, Florencio E Hernandez, and Gang Chen. 2020. Ultrasensitive visual detection of glucose in urine based on the iodide-promoted etching of gold bipyramids. *ACS Applied Materials & Interfaces* 12, 44 (2020), 49502–49509.

[39] Kamrun Nahar Fatema, Chang-Sung Lim, Yin Liu, Kwang-Youn Cho, Chong-Hun Jung, and Won-Chun Oh. 2022. 3D Modeling of silver doped ZrO2 coupled graphene-based mesoporous silica quaternary nanocomposite for a nonenzymatic glucose sensing effects. *Nanomaterials* 12, 2 (2022), 193.

[40] Weishan Shi, Jing Li, Jie Wu, Qianying Wei, Cuili Chen, Ning Bao, Chunmei Yu, and Haiying Gu. 2020. An electrochemical biosensor based on multi-wall carbon nanotube–modified screen-printed electrode immobilized by uricase for the detection of salivary uric acid. *Analytical and Bioanalytical Chemistry* 412 (2020), 7275–7283.

[41] Joris Penders, Tom Fiers, and Joris R. Delanghe. 2002. Quantitative evaluation of urinalysis test strips. *Clinical Chemistry* 48, 12 (2002), 2236–2241.

[42] Gennifer T Smith, Nicholas Dwork, Saara A Khan, Matthew Millet, Kiran Magar, Mehdi Javanmard, and Audrey K Ellerbee Bowden. 2016. Robust dipstick urinalysis using a low-cost, micro-volume slipping manifold and mobile phone platform. *Lab on a Chip* 16, 11 (2016), 2069–2078.

[43] Tianxing Li, Qiang Liu, and Xia Zhou. 2016. Practical human sensing in the light. In *Proceedings of the 14th Annual International Conference on Mobile Systems, Applications, and Services.* 71–84.

[44] Tianxing Li, Xi Xiong, Yifei Xie, George Hito, Xing-Dong Yang, and Xia Zhou. 2017. Reconstructing hand poses using visible light. *Proceedings of the ACM on Interactive, Mobile, Wearable and Ubiquitous Technologies* 1, 3 (2017), 1–20.

[45] Yichen Li, Tianxing Li, Ruchir A Patel, Xing-Dong Yang, and Xia Zhou. 2018. Self-powered gesture recognition with ambient light. In *Proceedings of the 31st annual ACM symposium on user interface software and technology.* 595–608.

[46] Zimo Liao, Zhicheng Luo, Qianyi Huang, Linfeng Zhang, Fan Wu, Qian Zhang, and Yi Wang. 2021. SMART: screen-based gesture recognition on commodity mobile devices. In *Proceedings of the 27th Annual International Conference on Mobile Computing and Networking.* 283–295.

[47] Tianxing Li, Qiang Liu, and Xia Zhou. 2017. Ultra-low power gaze tracking for virtual reality. In *Proceedings of the 15th ACM Conference on Embedded Network Sensor Systems.* 1–14.

[48] Tianxing Li and Xia Zhou. 2018. Battery-free eye tracker on glasses. In *Proceedings of the 24th Annual International Conference on Mobile Computing and Networking.* 67–82.

[49] Tianxing Li, Derek Bai, Temiloluwa Prioleau, Nam Bui, Tam Vu, and Xia Zhou. 2020. Noninvasive glucose monitoring using polarized light. In *Proceedings of the 18th conference on embedded networked sensor systems.* 544–557.

[50] Go Inamori, Umihiro Kamoto, Fumika Nakamura, Yutaka Isoda, Azusa Uozumi, Ryosuke Matsuda, Masaki Shimamura, Yusuke Okubo, Shuichi Ito, and Hiroki Ota. 2021. Neonatal wearable device for colorimetry-based real-time detection of jaundice with simultaneous sensing of vitals. *Science advances* 7, 10 (2021), eabe3793.

[51] Qianyi Huang, Zhice Yang, and Qian Zhang. 2018. Smart-U: smart utensils know what you eat. In *IEEE INFOCOM 2018-IEEE Conference on Computer Communications.* IEEE, 1439–1447.

[52] Hidenori Matsui, Takahiro Hashizume, and Koji Yatani. 2018. Al-light: An alcohol-sensing smart ice cube. *Proceedings of the ACM on interactive, mobile, wearable and ubiquitous technologies* 2, 3 (2018), 1–20.

[53] Haiyan Hu, Qian Zhang, and Yanjiao Chen. 2022. NIRSCam: A mobile near-infrared sensing system for food calorie estimation. *IEEE Internet of Things Journal* 9, 19 (2022), 18934–18945.

[54] Weiwei Jiang, Gabriele Marini, Niels van Berkel, Zhanna Sarsenbayeva, Zheyu Tan, Chu Luo, Xin He, Tilman Dingler, Jorge Goncalves, Yoshihiro Kawahara, et al. 2019. Probing sucrose contents in everyday drinks using miniaturized near-infrared spectroscopy scanners. *Proceedings of the ACM on Interactive, Mobile, Wearable and Ubiquitous Technologies* 3, 4 (2019), 1–25.

[55] Yongzhi Huang, Kaixin Chen, Lu Wang, Yinying Dong, Qianyi Huang, and Kaishun Wu. 2021. Lili: liquor quality monitoring based on light signals. In *Proceedings of the 27th Annual International Conference on Mobile Computing and Networking.* 256–268.